Latitude Distribution of Sunspots: Analysis Using Sunspot Data and a Dynamo Model

Sudip Mandal[1] , Bidya Binay Karak[2] , and Dipankar Banerjee[1,3]

[1] Indian Institute of Astrophysics, Koramangala, Bangalore 560034, India; sudip@iiap.res.in
[2] High Altitude Observatory, National Center for Atmospheric Research, 3080 Center Green Dr., Boulder, CO 80301, USA
[3] Center of Excellence in Space Sciences India, IISER Kolkata, Mohanpur 741246, West Bengal, India

Abstract

In this paper, we explore the evolution of sunspot latitude distribution and explore its relations with the cycle strength. With the progress of the solar cycle, the distributions in two hemispheres from mid-latitudes propagate toward the equator and then (before the usual solar minimum) these two distributions touch each other. By visualizing the evolution of the distributions in two hemispheres, we separate the solar cycles by excluding this hemispheric overlap. From these isolated solar cycles in two hemispheres, we generate latitude distributions for each cycle, starting from cycle 8 to cycle 23. We find that the parameters of these distributions, namely the central latitude (C), width (δ), and height (H), evolve with the cycle number, and they show some hemispheric asymmetries. Although the asymmetries in these parameters persist for a few successive cycles, they get corrected within a few cycles, and the new asymmetries appear again. In agreement with the previous study, we find that distribution parameters are correlated with the strengths of the cycles, although these correlations are significantly different in two hemispheres. The general trend features, i.e., (i) stronger cycles that begin sunspot eruptions at relatively higher latitudes, and (ii) stronger cycles that have wider bands of sunspot emergence latitudes, are confirmed when combining the data from two hemispheres. We explore these features using a flux transport dynamo model with stochastic fluctuations. We find that these features are correctly reproduced in this model. The solar cycle evolution of the distribution center is also in good agreement with observations. Possible explanations of the observed features based on this dynamo model are presented.

Key words: Sun: activity – Sun: magnetic fields – Sun: photosphere – sunspots

1. Introduction

A beautiful feature of the solar cycle is its latitude-time distribution, or the so-called butterfly diagram. At the beginning of the cycle, sunspots appear to be distributed around the mid-latitudes, and with the progress of the cycle, the distribution moves toward the equator. This is known as the equatorward migration of sunspots (Hathaway 2011). This feature of the solar cycle has become a central interest to many solar astronomers, as well as to dynamo modelers. As the strengths are not the same for all the cycles, sunspot latitudinal distributions are also expected to be different. However, evidence that the cycle strength has some relations with the properties of these distributions has been found. Solanki et al. (2000) identified a correlation between the cycle strength and the mean latitude of sunspot distribution. They showed even a stronger correlation between the width and the mean latitude of such a distribution. Later, using the group sunspot data, Li et al. (2003) showed that the number of sunspot group present at latitudes $\geqslant 35°$ is positively correlated with the amplitude of the cycle (also see Leussu et al. 2017). Finally, Solanki et al. (2008) computed various moments of sunspot distribution separately for two hemispheres and have shown that the three lowest moments (i.e., the total area covered by the sunspots over a cycle, the mean sunspot latitudes, and the width of the distribution) are well correlated with each other. Recently, Ivanov & Miletsky (2016) showed that the latitude properties of sunspot distribution are much more stable against the gaps of observations, and hence these properties can be used for estimates of quality of observations and for data series calibration.

Based on the polarities of the bipolar sunspot (the Hale polarity rule; Hale et al. 1919), it is believed that the sunspots

are produced from the toroidal (east–west directed) field underneath the surface. The sign of this toroidal field must be opposite in two hemispheres during a cycle and the polarity flips in every cycle. Thus, the propagation of the distribution of the sunspots at the surface is an observable of the equatorward migration of the toroidal field band, which is in the interior of the Sun. For this equatorward migration, two major explanations are available in the literature. One is due to the dynamo wave, whose direction of propagation is determined by signs of radial shear and α (the so-called Parker–Yoshimura sign rule), and other is due to the equatorward drift of the toroidal flux by an equatorward flow (meridional circulation and/or magnetic pumping). Based on theories and observations of the differential rotation, α effect, and the meridional circulation, we expect that the equatorward drift of the toroidal field by the flow is the cause of the propagation of the sunspot distribution in the Sun, although we do not want to exclude the other possibility, and in fact we do not have to debate this issue here (Karak & Cameron 2016; Cameron et al. 2017).

Recently, Cameron & Schüssler (2016) have identified the equatorward migration of the sunspot-producing toroidal field band from the equatorward migration of sunspot distribution (see also Hathaway 2011; Jiang et al. 2011). In each hemisphere, they have approximated sunspot latitudes for every year with a Gaussian distribution. For all cycles, Cameron & Schüssler (2016) have shown that this Gaussian in each hemisphere evolves separately, and depending on the strength of the cycle, the activity and the width of the Gaussian increase first and then decline at the same rates. They interpreted this result with the fact that in the solar interior two distinct toroidal flux bands in two hemispheres are transported toward the equator, and when these two bands

begin to touch each other, they cancel. This cancellation and the cross-equator diffusion of toroidal magnetic flux, which begin a few years before the usual solar minimum, are the processes in which the solar cycle interacts with the other hemisphere. In other words, there is a hemispheric overlap at the end of each cycle in contrast to the usual inter-cycle overlap, as emphasized by Cameron & Schüssler (2007).

In this manuscript, we isolate the solar cycle in each hemisphere by excluding the cancellation and the cross-equator diffusion of toroidal magnetic flux in two hemispheres by removing the hemispheric overlap and study the properties of the latitudinal distribution of the solar cycle. In previous studies (Solanki et al. 2000, 2008; Li et al. 2003), the solar cycles were separated only based on the usual inter-cycle overlap, and not the hemispheric overlap. We shall explore how the properties of sunspot distribution of the isolated solar cycle evolve in two hemispheres. Next, to study these features, we shall employ a Babcock–Leighton type flux transport dynamo model in which the toroidal flux near the bottom of the convection zone, which is assumed to produce sunspots at the surface, is transported toward the equator by an equatorward meridional flow. This dynamo model has become a popular paradigm in recent years for modeling the solar cycle at present (Karak et al. 2014; Choudhuri 2015). We show that by including fluctuations in the Babcock–Leighton process of this model, all the observed properties can be correctly reproduced.

2. Observational Data

In our study, we mainly use the Royal Greenwich Observatory (RGO) sunspot data.[4] This data, however, covers only from cycle 12 to cycle 23 (year 1874–2011) and thus to obtain the data for previous cycles, (i.e., cycles 7–11), we use the recently digitized sunspot catalog compiled by Leussu et al. (2017); see Centre de Données astronomiques de Strasbourg (CDS).[5] This data only provides the locations of sunspots from the digitized drawings of Schwabe (1826–1867) and Spörer (1866–1880). Since the early years of cycle 7 are not available in the Leussu et al. (2017) catalog, we shall begin our analysis from cycle 8. Although this new catalog contains data for up to the present cycle, for cycles 12–23, we still use RGO data, which is popular and has been used in many previous studies. We also make use of the sunspot number data provided by the Solar Influences Data Center (SIDC). This is the newly calibrate data[6] (V2.0).

3. Methods

As discussed in the introduction, our interest is to investigate the properties of sunspot latitude distribution of individual hemispheric cycle. Thus, for a given cycle, we restrict our analysis between the start of the cycle and the year when the two latitude distributions of two hemispheres come in contact with each other. This definition is motivated by Cameron & Schüssler (2016), and it allows us to capture the behavior of the isolated cycle, without having any influence from the other hemisphere. In our analysis, first we remove the inter-cycle overlap (Cameron & Schüssler 2007) by excluding one year at the beginning and one year at the end of the cycle. Next for every one-year data, we make the distribution of the sunspot latitudes, as shown in
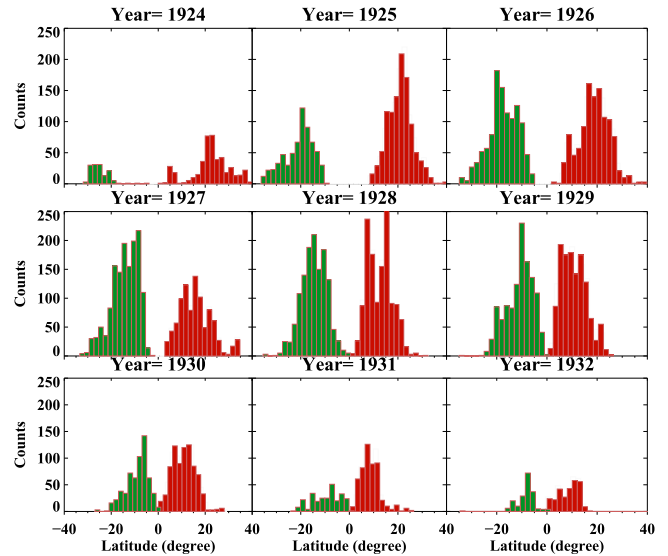

Figure 1. Latitude distributions of sunspots from 1924–1932 (i.e., covering most of the solar cycle 16). A bin size of 2° is used to compute the distributions. Red and green colors represent the northern and southern hemispheres, respectively.
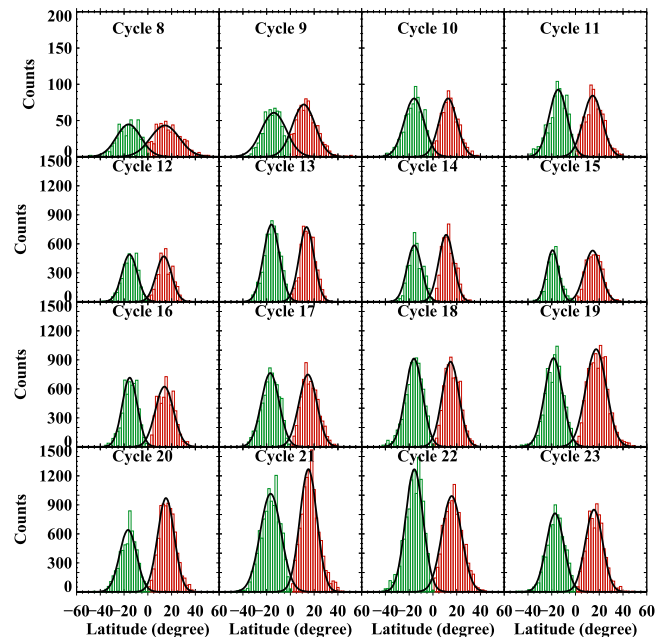

Figure 2. Histograms showing the latitude distributions of the sunspots for cycles 8–23. Red and Green colors highlight the northern and southern hemispheres. Black solid curves represent the fitted Gaussian functions on the individual hemispheric distributions.

Figure 1 for cycle 16. We observe that the separation between the two distributions is large in the beginning of the cycle (year 1924), and progressively this becomes narrower. Eventually, two distributions come in contact with each other (in year 1929). Thus, the duration of cycle 16 is considered as the interval between 1924–1929. The above procedure is repeated for all the other cycles. Identification of the year, when the two distributions come in contact with each other, has been done visually.

Next, for each hemisphere, we generate the combined latitude distributions by taking the data within the cycle duration, as identified above. These distributions for cycles 8–23 are displayed in Figure 2. We fit the hemispheric
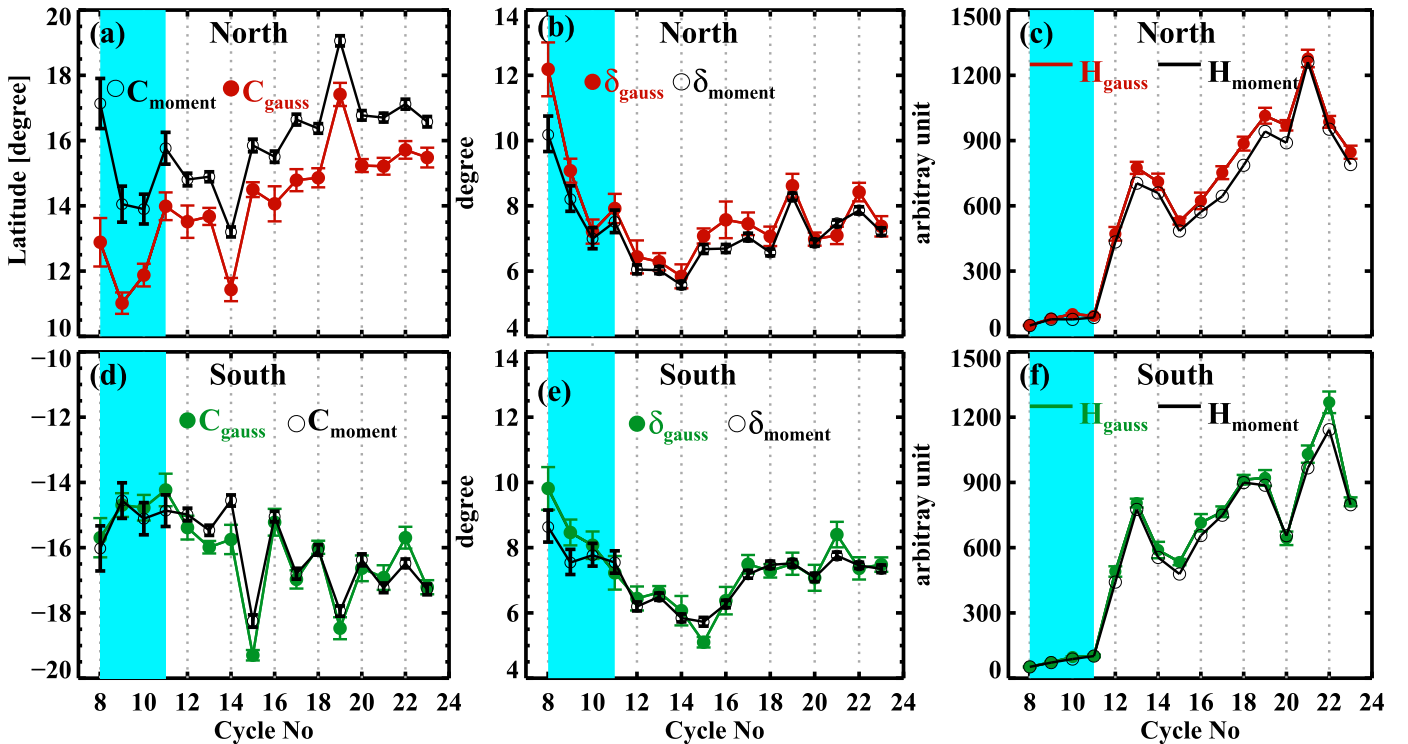
Figure 3. Left to right: evolutions of C, δ, and H computed from the latitude distributions (open circles) and from the fitted Gaussians (filled circles). The top and bottom panels are obtained from northern and southern hemispheres, respectively. The shaded region shows the data obtained from Leussu et al. (2017), while the unshaded region shows the result from RGO.

distributions with two individual Gaussians, as shown with the solid black lines in every panel of Figure 2. From every fitted Gaussians, we note three parameters: the height H_{Gauss} (in arbitrary unit), the central latitude C_{Gauss} (in degrees), and the width δ_{Gauss} (in degrees). In addition, we also calculate the mean C_{moment}, the standard deviation δ_{moment}, and the height of the distribution at the distribution mean H_{moment} directly from the original distributions. We note that when the distribution is perfectly Gaussian, parameters (C, δ, and H) obtained from these two methods must be identical.

4. Results

4.1. Evolutions of Distribution Parameters with Solar Cycle

In Figure 3, we display the evolutions of hemispheric C, δ, and H parameters, as obtained from the fitted Gaussians (filled points). The same parameters obtained from the distribution moments are also displayed (open circles) for comparison. The error bars on the Gaussian parameters represent the one sigma errors; whereas, for the distribution moments, it represents the 95% confidence interval of the derived quantity. We notice that the solar cycle variations of these parameters obtained from two methods follow similar patterns, although there are some differences in many cycles. Interestingly, we see many deviations in the northern hemisphere, as compared to the southern one. By seeing these significant differences, we can guess that the Gaussian profile does not fit the sunspot distribution adequately. To check the significance of the fitted Gaussian, we perform a normality test, "Shapiro–Wilk test," to all observed latitude distributions, and the results are presented in Table 1. This test, as proposed by Shapiro & Wilk (1965), calculates the W statistic whether or not a random sample comes from a normal distribution. A higher P value ($\geqslant 0.05$)

Table 1
Details from the Shapiro–Wilk Test

Cycle	Hemi-sphere	P	W	Hemi-sphere	P	W
8	N	0.0397	0.9169	S	0.0255	0.9066
9	N	0.0024	0.8653	S	0.0481	0.9084
10	N	0.1027	0.9196	S	0.0678	0.9156
11	N	0.1006	0.9191	S	0.0360	0.8964
12	N	0.1079	0.9150	S	0.0062	0.8571
13	N	0.0027	0.8456	S	0.0130	0.8806
14	N	0.0023	0.8422	S	0.0544	0.8985
15	N	0.0003	0.7357	S	0.0001	0.7086
16	N	0.0238	0.8872	S	0.0065	0.8467
17	N	0.0109	0.8844	S	0.0240	0.8972
18	N	0.0002	0.8173	S	0.0075	0.8770
19	N	0.0010	0.8485	S	0.0063	0.8770
20	N	0.0010	0.8344	S	0.0073	0.8800
21	N	0.0181	0.8946	S	0.0009	0.8544
22	N	0.0090	0.8870	S	0.0010	0.8484
23	N	0.0030	0.8625	S	0.0034	0.8683

along with a high W (>0.99) indicate that the "null-hypothesis" (that the sample is drawn from a normal distribution) cannot be rejected. We note that test is also applicable to a small sample size (Royston 1992). From the tabulated values, we note that only a few cycles (cycles 10, 11, 12, and 14) have a $P \geqslant 0.05$. Values of W are always lower than the critical value for all cycles. We thus conclude that the latitude distributions cannot be faithfully described by a Gaussian profile.

We would like to mention that despite poor a Gaussian fitting of the sunspot latitude distribution, many previous authors have used a Gaussian distribution. Particularly, Mandal et al. (2017) have shown that the latitude distribution of
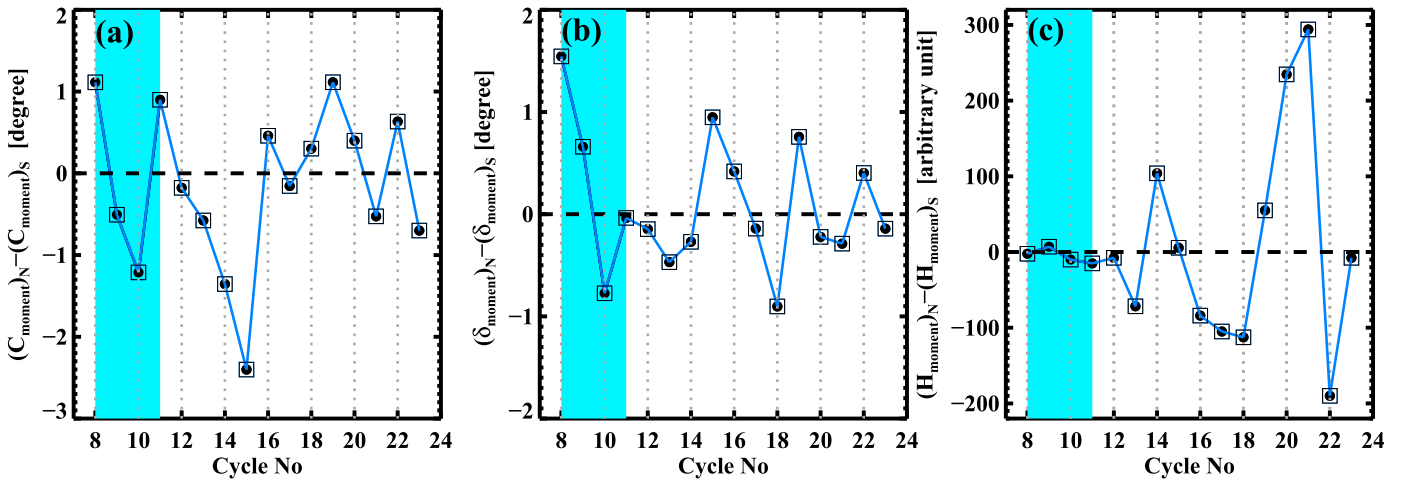
Figure 4. Different panels show the north–south asymmetry in the C_{moment}, δ_{moment}, and H_{moment} parameters.

sunspots in each hemisphere, integrated over the cycle length, follows a Gaussian distribution. Cameron & Schüssler (2016) have, in fact, used a Gaussian profile for the yearly sunspot data. There are also attempts to use a double-Gaussian model to express the latitude distributions (Chang 2012), whereas Miletsky et al. (2013) showed a significant skewness in the distribution and this skewness varies over the solar cycle. However, as in our study, we can obtain the required parameters of the sunspot distributions directly from the latitude distributions, and we shall only use C_{moment}, δ_{moment}, and H_{moment} for our further analysis. Thus, our computation of these parameters is essentially similar to that of Solanki et al. (2008).

Returning to the solar cycle variations of the sunspot latitude distribution in Figure 3, we find that C and H follow increasing trends with the cycle number. The most interesting feature we observe is the hemispheric asymmetry. For first few cycles, the variation of C is very different in two hemispheres. In the southern hemisphere, C does not increase much with the cycle number. Also, for C_S, there is a large peak in cycle 15, while for C_N, the largest peak is in cycle 19. Therefore, when we compute the difference of C_{moment} between two hemispheres, we obtain a nonzero value for most of the cycles; see Figure 4(a). The interesting behavior we see is that the asymmetry does not follow any particular pattern. For some cycles, C remains closer to the equator in the northern hemisphere, and then suddenly C becomes closer to the equator in the southern hemisphere. Although, for most of the cycles, the asymmetry persist for more than one cycle, and it gets corrected randomly and thus no hemisphere dominates permanently.

We mention that our result is very similar to the one obtained in Pulkkinen et al. (1999) and Zolotova et al. (2010) who presented the asymmetry of C, although the comparison is not straightforward. We recall that in the previous analyses, cycle lengths are computed from cycle minimum to minimum, while in our analysis, the length is defined by excluding the hemispheric overlap of sunspot distributions. Therefore, to check how our $C_N - C_S$ is affected by the definition of the cycle length, we repeat our analysis by defining the cycle length, as was done in Pulkkinen et al. (1999), and the result is shown in Figure 5. In this figure, we see a different variation.
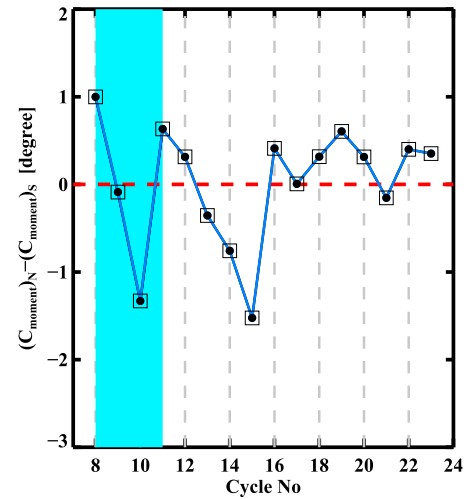

Figure 5. Same as in Figure 4(a), but in this case, the cycle length is computed from the interval between the cycle beginning and end (i.e., it does not exclude the hemispheric overlap).

For a few cycles, the sign of $C_N - C_S$ changed compared to the one found in Figure 4(a), although the overall variation is not very different. Keeping in mind that our analysis contains a longer data and C_N and C_S are computed over one-cycle data, the variation of $C_N - C_S$ obtained in Figure 5 is equivalent to that found in Figure 4 of Pulkkinen et al. (1999).

Now we go back to Figure 3(b) to follow the evolution of δ in the two hemispheres. We find that for cycle 8, δ is significantly higher compared to all other cycles. One possible reason for this could be the sparse data during this cycle, resulting larger error bar too. We also find a significant hemispheric asymmetry in δ, as shown in Figure 4(a). In this case, $\delta_N - \delta_S$ shows some oscillations around zero. However, given the limited data, we cannot confirm any periodicities that might exist in $\delta_N - \delta_S$. Interesting, this asymmetry tends to decrease with the cycle number.

In Figure 3(c), the variation of H parameter shows a similar trend in two hemispheres except for a few cycles. Particularly, H has the highest peak for cycle 21 in the northern hemisphere, while in the southern hemisphere, the highest
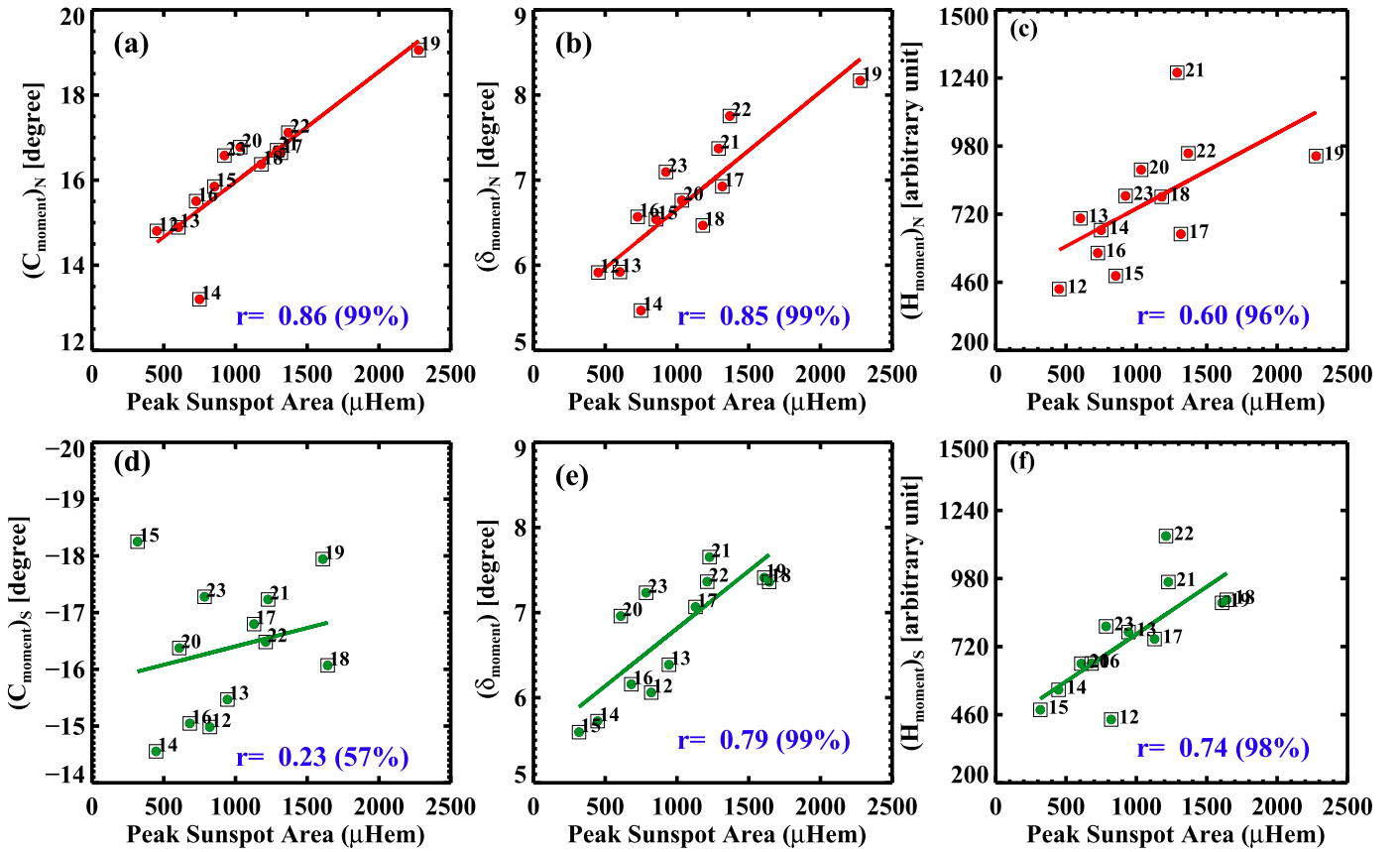
Figure 6. Left to right: scatter plots of C, δ, and H with the peak sunspot area. The top and bottom (green) panels represent the values obtained for the northern and southern hemispheres, respectively. The linear Pearson correlation coefficients (r) between parameters (along with the confidence levels) are printed on each panel.

peak is in cycle 22. Similar to other parameters, we do find a considerable hemispheric asymmetry. However, unlike δ, H shows higher asymmetry during recent cycles.

4.2. Correlations between Cycle Strength and Distribution Parameters

4.2.1. Considering Hemispheric Data

We now demonstrate the dependence of these distribution parameters with the cycle strength. In Figure 6, we show the scatter plots of C_{moment}, δ_{moment}, and H_{moment} with the peak sunspot area. The linear Pearson correlation coefficients are also displayed in these plots. Correlations using the Gaussian parameters are also computed and are summarized in Table 2 for comparison. We note that in these correlations plots, we have used the peaks of yearly sunspot area data as measures of the cycle strengths because no homogeneous, long-term hemispheric sunspot number data is available before 1992. We also note that in the correlation plots, we do not consider the data of Leussu et al. (2017) for cycles 8–11. We already noticed in Figure 3 that although the Leussu et al. (2017) catalog provides data from cycle 8, this data is very different than RGO data. We realize that the number of spots for a given day is different than that provided by the RGO record. Although C and δ parameters are less affected by such discrepancies, the H parameter, which has a strong dependency on the number of spots, is significantly affected (see the sudden increase in Figure 3(c) for H in cycle 12). Therefore, if we include cycles 8–11 data in our correlation analysis, then some

of the results get spoiled; see Table 2. Furthermore, since we do not have systematic area measurements prior to cycle 12, the computation of correlations in this case are restricted to cycles 12–23.

In Figure 6, we observe a significant positive correlation ($r = 0.86$) between C_N and the peak sunspot area. However, the same correlation is insignificant in the southern hemisphere ($r = 0.23$). This correlation does not improve when computed using the C_{Gauss} data (Table 2). Even when this correlation is computed using the data of Leussu et al. (2017) for all cycles, the correlation is weaker in the southern hemisphere.

We note that our result is in agreement with Leussu et al. (2017), who also find a weak correlation between the first sunspot latitudes (they call it the first latitude) and the wing strengths, and no correlation between the latitudes of the last sunspot groups (end of the wing) and the wing strengths. Interestingly, Solanki et al. (2008) found a stronger correlation between the total sunspot area and C_{moment} in the southern hemisphere. Thus, the correlation between C and cycle strength is very sensitive to how we separate the individual cycle. Interestingly, the correlations between δ_{moment} and the cycle strength is significant in both hemispheres (Figures 6(b) and (e)). Our correlation values are comparable to the ones obtained in Solanki et al. (2008). Slight differences are, again, due to the definition of the cycle length used to generate the latitude distributions here.

Next, we explore what determines the higher H of the latitude distribution. There are two reasons for having a higher H of the distribution: (i) a larger number of sunspots, or (ii) a small δ value. However, when we compute the correlation
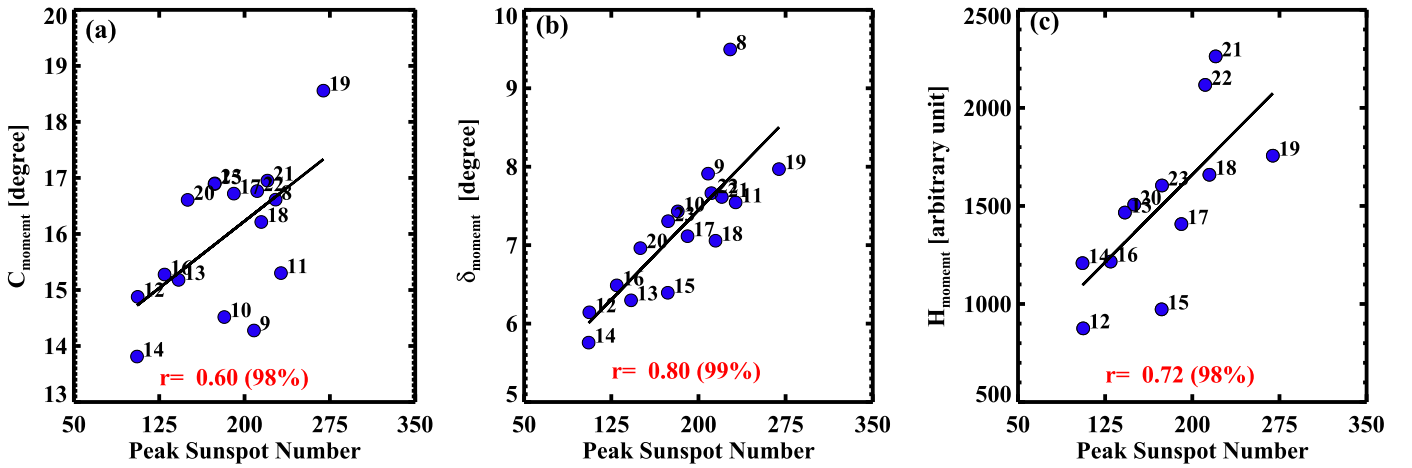
Figure 7. Same as in Figure 6, but distribution parameters that are obtained from the unsigned latitudes (full disc), and the horizontal axes represent the peak sunspot number.

Table 2
The Linear Pearson Correlation Coefficients (r) and the Confidence Levels between Various Parameters

Parameters	Hemisphere	r_{moment}	r_{Gauss}
Data source: RGO (12 − 23)			
C versus (sunspot Area)$_{\mathrm{peak}}$	N	0.86 (99%)	0.80 (99%)
	S	0.23 (57%)	−0.02 (06%)
δ versus (sunspot Area)$_{\mathrm{peak}}$	N	0.85 (99%)	0.78 (99%)
	S	0.79 (99%)	0.72 (98%)
H versus (sunspot Area)$_{\mathrm{peak}}$	N	0.60 (96%)	0.64 (97%)
	S	0.74 (98%)	0.70 (98%)
Data source: Leussu et al. (8 − 11) + RGO (12 − 23)			
C versus (sunspot Number)$_{\mathrm{peak}}$	combined	0.60 (98%)	0.33 (81%)
δ versus (sunspot Number)$_{\mathrm{peak}}$	combined	0.80 (99%)	0.66 (99%)
H versus (sunspot Number)$_{\mathrm{peak}}$	combined	0.72 (98%)	0.74 (98%)
Data source: Leussu et al. (12 − 23)			
C versus (sunspot Area)$_{\mathrm{peak}}$	N	0.78 (99%)	0.59 (95%)
	S	0.40 (83%)	0.19 (48%)
δ versus (sunspot Area)$_{\mathrm{peak}}$	N	0.84 (99%)	0.73 (98%)
	S	0.58 (95%)	0.67 (97%)
H versus (sunspot Area)$_{\mathrm{peak}}$	N	−0.15 (39%)	−0.07 (18%)
	S	0.26 (63%)	0.30 (69%)
Data source: Leussu et al. (8 − 23)			
C versus (sunspot Number)$_{\mathrm{peak}}$	combined	0.60 (98%)	0.36 (81%)
δ versus (sunspot Number)$_{\mathrm{peak}}$	combined	0.76 (99%)	0.67 (99%)
H versus (sunspot Number)$_{\mathrm{peak}}$	combined	−0.21 (64%)	−0.20 (57%)

between H_{moment} and δ_{moment}, we find positive correlations. The linear correlation coefficients (and confidence levels) are 0.64 (97%) and 0.84 (99%) for northern and southern hemispheres, respectively. However, in both hemispheres we get a positive correlation between H_{moment} and the cycle strength (Figures 6(c) and (f)). As discussed earlier, if the spot number is different in Leussu et al. (2017) data, then this correlation completely disappears when we consider this data; see the second row of Table 2. However, based on the

correlations obtained from RGO data, we confirm that stronger cycles with higher H have bigger distribution widths.

4.2.2. Merging the Hemispheres

We now explore whether or not the previous correlations obtained from individual hemispheric parameters survive when we combine the two hemispheres. To do so, we compute distributions from the unsigned latitudes of sunspots. Similar to the previous analysis, we compute various moments from these distributions and the correlation plots between the cycle strengths, and these distributions parameters are shown in Figure 7. We note that now we do not need hemispheric data, and thus we take the peak sunspot number as the strength of the solar cycle, instead of sunspot areas that we have considered in the previous section. As seen in Figure 7, significant positive correlations exist for all parameters. Therefore, we confirm that stronger cycles have higher mean latitudes, widths, and peaks of the distributions.

5. Results Using a Flux Transport Dynamo Model

To explore above features of the solar cycle in a theoretical model, we consider a Babcock–Leighton type flux transport dynamo model (Choudhuri et al. 1995; Dikpati & Charbonneau 1999). In this study, we consider the same dynamo model used in Karak & Choudhuri (2011). The original model was developed by Nandy & Choudhuri (2002) and Chatterjee et al. (2004), and later this model was used in many studies (see a review by Choudhuri 2015). Thus, without providing the details of this model in the present study, we mention the salient features of this model.

This is an axisymmetric dynamo model in which the poloidal and toroidal components of the magnetic field are evolved with a given axisymmetric velocity field. In this model, the toroidal field is produced from the poloidal field through differential rotation in the convection zone, while the poloidal field is produced near the solar surface from the toroidal field at the base of the convection zone through an α effect. This α essentially captures the Babcock–Leighton process in which tilted bipolar sunspots decay and disperse to produce poloidal field on the solar surface. This model also includes a single-cell (in each hemisphere) meridional flow such that it is poleward in the upper half of the convection zone and equatorward in the
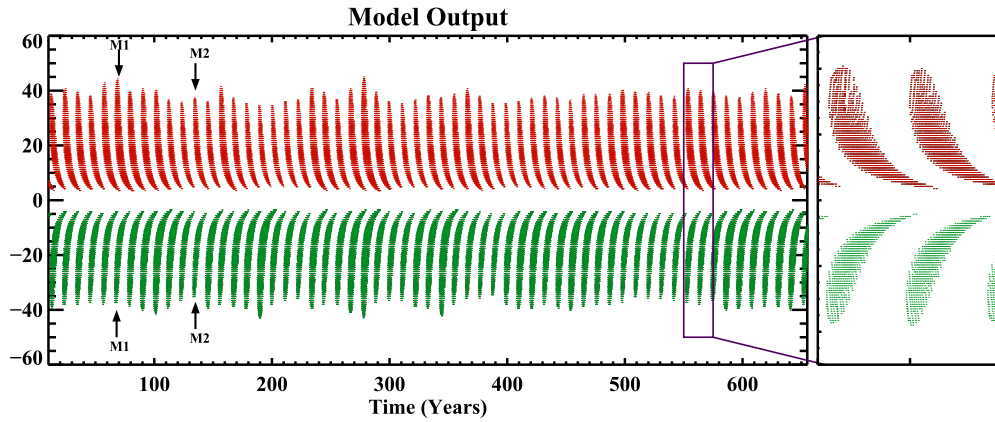
Figure 8. Butterfly diagram generated using a Babcock–Leighton type flux transport dynamo model. The inset box shows a zoomed in view of the diagram for a better visualization. Two arrows highlight the cycles used to generate Figure 9.

lower half. This model reproduces the regular solar cycle when the flow and the α are fixed.

In this flux transport dynamo model, the poloidal flux can be changed due to multiple reasons. The main reason for this is the fluctuations in the Babcock–Leighton process through the observed variations in the tilt angle around Joy's law (Dasi-Espuig et al. 2010; Stenflo & Kosovichev 2012; Jiang et al. 2014; Karak & Miesch 2017). Thus, to capture the variation in the poloidal flux and to produce irregular solar cycles in this model, we follow the same procedure prescribed by Choudhuri et al. (2007). At the end of every solar cycle when polar field reaches to its maximum value in this model, we change the poloidal field above $0.8R_\odot$ by a factor γ, where γ is obtained randomly from a uniform distribution within [0.5, 1.5]. We do this change independently in two hemispheres because the randomness in the Babcock–Leighton process is uncorrelated in the hemispheres.

We run the model for 93 cycles by changing the polar field at each solar minimum, and the butterfly diagram of model sunspot eruptions is shown in Figure 8. As we can see from this diagram, most of the basic features of the solar cycle are reproduced in this model. We also notice that for some cycles, sunspots start appearing at somewhat higher latitudes. It turns out that for stronger cycles (e.g., Cycle M1, as shown by the first arrow in Figure 8), the first latitudes of a sunspot appearance happen at relatively higher latitudes, and vice versa. This is in good agreement with the observation illustrated by Leussu et al. (2017) in a detailed analysis. However, there are some minor differences between the model and observed butterflies. Particularly, in the model, no spots are produced within $\pm5°$ latitudes (see Figure 8), while in observations, we even find spots close to the equator. Therefore, we have fewer data points near the equator of the histograms, as shown in Figure 9, and thus the distributions look more skewed than the observed one.

From the model latitude distributions, we compute C_{moment}, δ_{moment}, and H_{moment} for all cycles in the same way as done for the observed data. The correlation plots between various quantities are plotted in Figure 10. Strikingly, all of the correlations found in observations (Figures 6 and 7) are beautifully reproduced in both hemispheres. See the correlation coefficients and confidence levels printed on the plot. For the full disc data, the correlation coefficients (confidence levels) of
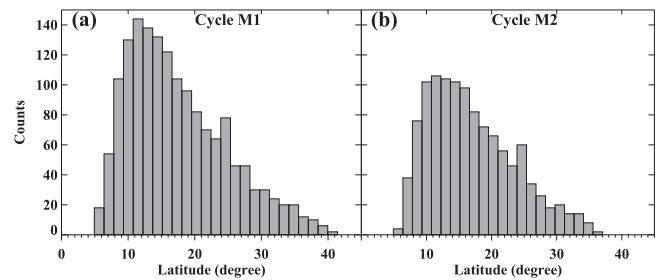

Figure 9. Representative example of the latitude distributions obtained using the dynamo model (cycles are highlighted by arrows in Figure 8).

cycle strength with C, δ and H are 0.90 (99.9%), 0.95 (99.9%), and 0.88 (99.9%), respectively.

The correlation between the center and the peak sunspot number is understood in the following way. In our model, the poloidal field is produced near the surface at low latitudes. This field is advected toward the higher latitudes (due to the poleward flow) and then down to the bottom of the convection zone (due to the downward flow). In this process, the diffusion also contributes to transport the poloidal field from the surface to the deeper convection zone. The poloidal field then produces toroidal field through the differential rotation. This toroidal field is transported to the low latitudes by the equatorward meridional flow and produces sunspot eruptions when it exceeds a certain value. This is how we get spots below about $\pm30°$ latitudes. However, due to fluctuations in the poloidal field generation process, when the toroidal field becomes strong, it starts exceeding the field strength for spot eruption at somewhat higher latitudes before reaching lower latitudes. This allows the model to start spot eruptions at relatively higher latitudes. Thus, for the stronger cycles (with more sunspot eruptions), eruptions begin at slightly higher latitudes. This causes a positive correlation between the peak sunspot numbers and the centers of sunspot latitudes (C). Furthermore, for stronger cycles, when sunspot eruptions start from higher latitudes, the overall latitude extents of sunspots are increased and thus the widths of distributions are increased. This explains the positive correlation between the peak sunspot numbers and δ.

We remember that so far we have obtained all of the parameters (C, δ and H) averaged over each cycle. These parameters, however, have variations within the cycle. Cameron & Schüssler (2016) have studied the evolution of C
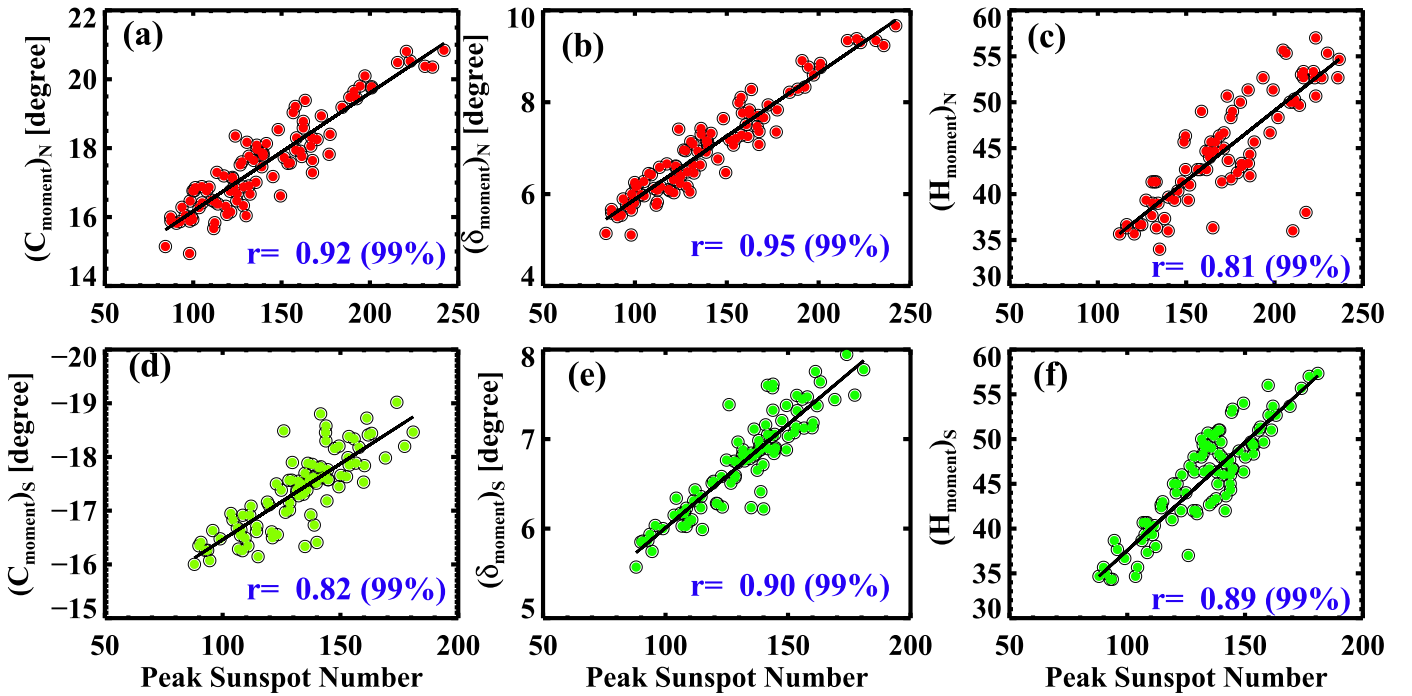
Figure 10. Scatter plots showing the correlations of C_{moment}, δ_{moment}, and H_{moment}, with the peak spot numbers, as obtained from the dynamo model. The top and bottom panels are obtained from the northern and southern hemispheres, respectively.

of the fitted Gaussians as functions of the cycle phase. They have shown that all cycles begin at different latitudes. Depending on the strengths, their activity levels first rise to highest values, and then they all decay at the same rate; see their Figure 3. To check whether our model reproduces this feature or not, we repeat the same analysis. We note that Cameron & Schüssler (2016) fitted the latitudinal distribution of sunspots with the Gaussian profile and obtained the center C. However, as discussed in Section 4.1, the Gaussian does not statistically fit the latitude distribution, particularly for our model where the fitting will be even worse. Therefore, we obtain the centers' C_{moment} directly from the latitude distribution. We compute this from each one-year data for every cycle in each hemisphere. The variation of this C_{moment} with the total number of spot in each year is shown in Figure 11. Thus, in this plot, each curve represents the evolution of the center of the latitude distribution with the number of spots in each year. Every point in the plot corresponds to one-year data. It is obvious that cycle begin from the right bottom corner. Then with the progress of the cycle, the spot number increases first and then decreases. The cycle eventually ends at the left bottom corner. The interesting features, as emphasized in Cameron & Schüssler (2016), is that different cycles begin at different latitudes, and depending on the cycle strength, they rise at different rates. In Figure 11, we see that stronger cycles (red and brown lines) begin at higher latitudes, and they rise fast (the Waldmeier effect—Waldmeier 1935; Karak & Choudhuri 2011) and begin to fall earlier (at higher latitudes). Whereas weaker cycles (cyan and blue lines) rise slowly and begin to fall later (at lower latitudes) compare peaks of all curves. Therefore, the most interesting fact is that although different cycles rise differently (given by the Waldmeier rule), they all fall at the same rate. In summary, the evolution of the latitudinal distribution of our model spot-latitudes is in good agreement with the observed behavior, as shown in Cameron & Schüssler (2016).
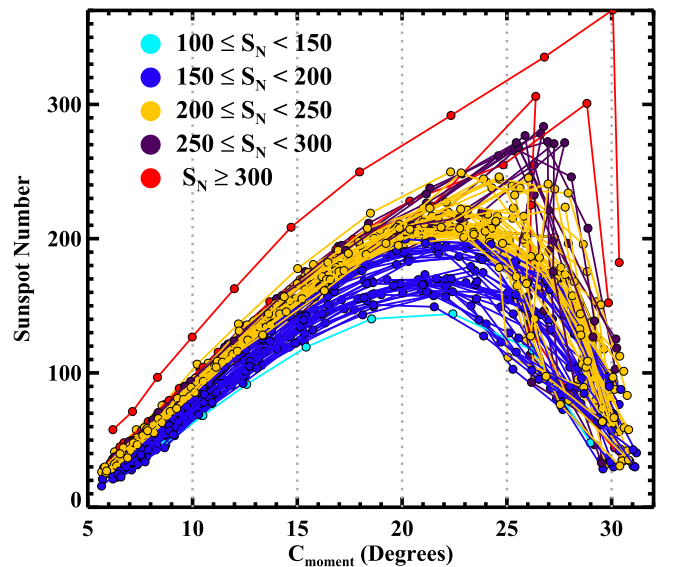

Figure 11. Trajectories of the centers (*C*) of the latitude distributions of yearly spot numbers plotted with the number of spots in each year of the cycle. Thus, each point corresponds to one-year data, and each curve corresponds to one cycle. The cycle begins from right and ends on the left. Cycles are colored based on their strength (as measured by the peak spot number). These classifications are printed on the plot.

6. Conclusion and Discussion

We have analyzed the latitude distributions of sunspots over the past 16 solar cycles, which includes the newly digitized sunspot data from Schwabe and Spörer, and RGO records. In our study, we define the cycle length carefully by excluding the hemispheric overlap that might occur during the solar minimum, as described in Cameron & Schüssler (2016). Thus, in our study, we capture the true hemispheric properties of the sunspot distributions that are free from any influence of the

other hemisphere. We show that the latitude distribution of sunspots does not statistically follow a Gaussian distribution. Distribution parameters, namely H, C, and δ, show significant positive correlations with the cycle strengths. These correlations are in general agreement with the previous findings of Solanki et al. (2008), although there are some differences in the values of the correlations, as the cycle lengths are computed differently in their study. In general, the observed correlations imply that stronger cycles begin sunspot eruptions at relatively higher latitudes, and they have wider extends of sunspot eruption latitudes. Another interesting result from this study is the hemispheric asymmetry in the distribution parameters, especially in the center values (C). We find that the $C_N - C_S$ parameter oscillates around the zero value, whereas the amplitude of this oscillation seems to decrease with the increase of the cycle number.

To explore these features, we have applied a flux transport dynamo model in which polar field at the solar minimum is varied randomly. Although this model produces many features of the solar cycle correctly, the latitudinal distribution of sunspots is not in good agreement with observation because of the fewer sunspots near the equator. Despite of this dissimilarity, all correlations among the distribution parameters, as obtained in observation, are reproduced correctly. Our results are in broad agreement with that of Solanki et al. (2008), who reproduced similar correlations using a simplified thin shell dynamo model. While our model has a fixed single-cell (in each hemisphere) meridional flow, Solanki et al. (2008) showed that the model with and without meridional flow produce slightly different results. Our model also reproduces the detailed variation of these parameters within the cycle, as demonstrated by Cameron & Schüssler (2016). Thus, our study supports a considerable variation in the polar field as the cause of the irregular solar cycle and variations in the latitude distributions.

The variation in the polar field is directly and indirectly observed in the Sun (Muñoz-Jaramillo et al. 2013; Priyal et al. 2014). This variation is primarily caused by the the scatter in the tilt angles of active regions around Joy's law (Cameron et al. 2013; Jiang et al. 2014; Hazra et al. 2017; Karak & Miesch 2017), which is actually observed in the Sun (e.g., Dasi-Espuig et al. 2010; Stenflo & Kosovichev 2012). While it is known that the variation in the meridional flow is expected to cause some variations in the solar cycle (e.g., Karak & Choudhuri 2011; Belucz & Dikpati 2013), due to difficulties in the measurements, we are uncertain about the amount of variation present in the deep meridional flow. However, the surface meridional flow is observed to change with the solar cycle and most of this variation is probably caused by the inflows around the active regions (Gizon et al. 2010). This meridional flow perturbation can change the polar field from cycle to cycle (Jiang et al. 2010; Hathaway & Upton 2014; Shetye et al. 2015). In our study, we have not considered how the polar field could be varied in cycle to cycle. This could be due to the observed tilt scatter around Joy's law and/or due to the variation in the surface meridional flow.

ORCID iDs

Sudip Mandal ⬤ https://orcid.org/0000-0002-7762-5629
Bidya Binay Karak ⬤ https://orcid.org/0000-0002-8883-3562
Dipankar Banerjee ⬤ https://orcid.org/0000-0003-4653-6823

References

Belucz, B., & Dikpati, M. 2013, ApJ, 779, 4
Cameron, R., & Schüssler, M. 2007, ApJ, 659, 801
Cameron, R. H., Dasi-Espuig, M., Jiang, J., et al. 2013, A&A, 557, A141
Cameron, R. H., Dikpati, M., & Brandenburg, A. 2017, SSRv, 210, 367
Cameron, R. H., & Schüssler, M. 2016, A&A, 591, A46
Chang, H.-Y. 2012, NewA, 17, 247
Chatterjee, P., Nandy, D., & Choudhuri, A. R. 2004, A&A, 427, 1019
Choudhuri, A. R. 2015, JApA, 36, 5
Choudhuri, A. R., Chatterjee, P., & Jiang, J. 2007, PhRvL, 98, 131103
Choudhuri, A. R., Schüssler, M., & Dikpati, M. 1995, A&A, 303, L29
Dasi-Espuig, M., Solanki, S. K., Krivova, N. A., Cameron, R., & Peñuela, T. 2010, A&A, 518, A7
Dikpati, M., & Charbonneau, P. 1999, ApJ, 518, 508
Gizon, L., Birch, A. C., & Spruit, H. C. 2010, ARA&A, 48, 289
Hale, G. E., Ellerman, F., Nicholson, S. B., & Joy, A. H. 1919, ApJ, 49, 153
Hathaway, D. H. 2011, SoPh, 273, 221
Hathaway, D. H., & Upton, L. 2014, JGRA, 119, 3316
Hazra, G., Choudhuri, A. R., & Miesch, M. S. 2017, ApJ, 835, 39
Ivanov, V. G., & Miletsky, E. V. 2016, Ge&Ae, 56, 848
Jiang, J., Cameron, R. H., Schmitt, D., & Schüssler, M. 2011, A&A, 528, A82
Jiang, J., Cameron, R. H., & Schüssler, M. 2014, ApJ, 791, 5
Jiang, J., Işik, E., Cameron, R. H., Schmitt, D., & Schüssler, M. 2010, ApJ, 717, 597
Karak, B. B., & Cameron, R. 2016, ApJ, 832, 94
Karak, B. B., & Choudhuri, A. R. 2011, MNRAS, 410, 1503
Karak, B. B., Jiang, J., Miesch, M. S., Charbonneau, P., & Choudhuri, A. R. 2014, SSRv, 186, 561
Karak, B. B., & Miesch, M. 2017, ApJ, 847, 69
Leussu, R., Usoskin, I. G., Senthamizh Pavai, V., et al. 2017, A&A, 599, A131
Li, K. J., Wang, J. X., Zhan, L. S., et al. 2003, SoPh, 215, 99
Mandal, S., Hegde, M., Samanta, T., et al. 2017, A&A, 601, A106
Miletsky, E. V., Ivanov, V. G., & Nagovitsyn, Y. A. 2013, Ge&Ae, 53, 962
Muñoz-Jaramillo, A., Dasi-Espuig, M., Balmaceda, L. A., & DeLuca, E. E. 2013, ApJL, 767, L25
Nandy, D., & Choudhuri, A. R. 2002, Sci, 296, 1671
Priyal, M., Banerjee, D., Karak, B. B., et al. 2014, ApJL, 793, L4
Pulkkinen, P. J., Brooke, J., Pelt, J., & Tuominen, I. 1999, A&A, 341, L43
Royston, P. 1992, Stat. Comp., 2, 117
Shapiro, S. S., & Wilk, M. B. 1965, Biometrika, 52, 591
Shetye, J., Tripathi, D., & Dikpati, M. 2015, ApJ, 799, 220
Solanki, S. K., Fligge, M., Pulkkinen, P., & Hoyng, P. 2000, JApA, 21, 163
Solanki, S. K., Wenzler, T., & Schmitt, D. 2008, A&A, 483, 623
Stenflo, J. O., & Kosovichev, A. G. 2012, ApJ, 745, 129
Waldmeier, M. 1935, Mitt. Eidgen. Sternw. Zurich, 14, 105
Zolotova, N. V., Ponyavin, D. I., Arlt, R., & Tuominen, I. 2010, AN, 331, 765